Full-Band Quantum Transport Simulation Based on Tight-Binding Green's Function Method

Matsuto Ogawa, Takashi Sugano, Ryuichiro Tominaga, and Tanroku Miyoshi

Department of Electrical and Electronics Engineering
Kobe University, 1 Rokkodai, Nada, Kobe 657-8501, Japan
Phone & Facsimile: +81-78-803-6074
E-mail: ogawa@eedept.kobe-u.ac.jp

Modeling and formulation of full-band quantum transport based on a non-equilibrium tight-binding Green's function method are presented where realistic band structures, evanescent-mode matching, space charge effect, and scattering effects are taken into account. Our results show that current-voltage characteristics of a GaAs/AlAs double-barrier RTD have larger current densities than the conventional single band model since the latter model is found to overestimate the decay constant in the barriers. It should be also noted that the full-band nature and polar optical phonon scattering effects significantly change the results of conventional RTD simulations.

1. Introduction

Electron tunneling in semiconductor heterostructures has been extensively studied for both its underlying physics and its device applications such as high-speed digital circuits since the first observation in a double-barrier resonant-tunneling diode (DBRTD) [1]. For comprehensive understanding of device physics, many assumptions, *e.g.*, the use of effective-mass single band structure model, the Esaki-Tsu current density formula, and Thomas-Fermi (T-F) charge screening, have been widely used in conventional simulations. However, in order to simulate quantum transport of carriers in present quantum devices more realistically and quantitatively, we have to avoid such assumptions, since experimental results often reflect the effects of nonparabolicity and multiple valleys of the realistic band[2, 3].

In this paper, we will present quantum transport modeling based on a non-equilibrium Green's function method. In the formulation, we adopt full-band (FB) treatment based on a tight binding theory to include the valley-mixing and nonparabolicity effects, in addition, possible existence of evanescent modes[4, 5] at heterointerfaces. The effect of polar-optical phonon scattering and interface roughness scattering are also included in the calculation through self-energy terms.

In the next section, we will briefly explain the full-band tight-binding Green's function method. In section 3, we will discuss our results and finally we will summarize our conclusion.

2. Evanescent Waves and Green's Functions

The Hamiltonian of DBRTD system generally has the form

$$H_0 = H_0^D + H_0^L + H_0^R + H_0^{LD} + H_0^{RD}, \qquad (1)$$

where H_0^D is the Hamiltonian of the device, H_0^L that of the left reservoir, and H_0^{LD} denotes the coupling of the left contact to the device, and so on. We confine ourselves to the analysis of carrier transport in the [0 0 1] direction in zinc-blende crystals. Then we can use an empirical tight-binding model with a basis of five orbitals per atom (s, p_x, p_y, p_z, s^*) assuming nearest neighbor overlaps, where s^* implies an excited s-state which includes the interaction from inner shells. The total electron wave function can be expressed in terms of the Bloch sum of the anion (a) and cation (c) states as

$$|\Psi(k_z, \boldsymbol{k}_\parallel, z)\rangle = \sum_{l,\alpha^a,\alpha^c} \left[c_{l\alpha^a}(k_z)|\boldsymbol{k}_\parallel, l, \alpha^a\rangle + c_{l\alpha^c}(k_z)|\boldsymbol{k}_\parallel, l, \alpha^c\rangle \right], \qquad (2)$$

where $|\boldsymbol{k}_\parallel, l, \alpha^j\rangle$ denotes a Bloch sum of α^j-like ($j = a, c$) atomic orbitals associated with the in-plane wave vector $\boldsymbol{k}_\parallel$, k_z the wave vector in propagating direction, l labels the index of the layer comprised of both the anion and cation atoms. Substituting $|\Psi(k_z, \boldsymbol{k}_\parallel, z)\rangle$ into the Schrödinger equation

$(H_0^{L(R)} - E)|\Psi(k_z, \boldsymbol{k}_\parallel, z)\rangle = 0$, where E is electron energy, yields an eigenvalue equation for electron waves existing in the left (or right) electrode crystal. Projecting the resulting equation in atomic orbitals located at atomic layer l leads to an equation relating the coefficients at layer $l+1$ to those at layers l and $l-1$. Finally we can express the eigenvalue equation with the aid of transfer matrices as

$$T\boldsymbol{C} = \exp(ik_z\Delta)\,\boldsymbol{C}, \tag{3}$$

where Δ is atomic monolayer spacing,

$$T \equiv T_c T_a, \tag{4}$$

$$T_j = \begin{bmatrix} -[H^{(+)}(l)]^{-1}H^{(0)}(l) & \\ 1 & \\ -[H^{(+)}(l)]^{-1}H^{(-)}(l) & \\ 0 & \end{bmatrix} \quad (j = a, c), \tag{5}$$

and $\boldsymbol{C}$ is a vector of coefficients defined by

$$\boldsymbol{C}^T(l) = (\ c_l^{sa}, c_l^{p_x a}, c_l^{p_y a}, c_l^{p_z a}, c_l^{s^* a}, c_l^{sc}, c_l^{p_x c}, c_l^{p_y c}, c_l^{p_z c}, c_l^{s^* c}), \tag{6}$$

and $H^{(+)}$,$H^{(0)}$, and $H^{(-)}$ are matrices with

$$H^{(+)}(l)_{\alpha^j\alpha'^j} = \langle \boldsymbol{k}_\parallel, l, \alpha^j | H | \boldsymbol{k}_\parallel, l+1, \alpha'^j \rangle, \tag{7}$$

$$H^{(0)}(l)_{\alpha^j\alpha'^j} = \langle \boldsymbol{k}_\parallel, l, \alpha^j | H | \boldsymbol{k}_\parallel, l, \alpha'^j \rangle - E\delta_{\alpha^j\alpha'^j}, \tag{8}$$

$$H^{(-)}(l)_{\alpha^j\alpha'^j} = \langle \boldsymbol{k}_\parallel, l, \alpha^j | H | \boldsymbol{k}_\parallel, l-1, \alpha'^j \rangle. \tag{9}$$

Since the transfer matrix T is a function of E, the eigenvalue equation (3) can be solved to find the *complex* energy-band diagram as well as the evanescent electron waves in the reservoir.

In our calculation, two non-equilibrium Green's functions, $G^<$ and G^R, are used for the analysis of quantum transport in the device. Assuming these expansion coefficients $c_{L,\alpha^j,\boldsymbol{k}_\parallel}$'s are field operators, the Green's functions in the multiband space are defined as

$$G^<_{\alpha,L,\alpha',L'}(\boldsymbol{k}_\parallel; t, t') = \frac{i}{\hbar}\langle c^\dagger_{\alpha',L',\boldsymbol{k}_\parallel}(t') c_{\alpha,L,\boldsymbol{k}_\parallel}(t)\rangle,$$

$$G^R_{\alpha,L,\alpha',L'}(\boldsymbol{k}_\parallel; t, t') = \theta(t-t')\left[G^>_{\alpha,L,\alpha',L'}(\boldsymbol{k}_\parallel; t, t') - G^<_{\alpha,L,\alpha',L'}(\boldsymbol{k}_\parallel; t, t')\right], \tag{10}$$

where $\theta(t-t')$ is a step function and L denotes the index of a layer comprised of both the anion and cation atoms, that is $\{l, l+1\} \in L$. We follow the treatment of the Dyson equations by Caroli [6] and its extension to the FB space by Lake [7]. The equation of motion for $G^<$ and G^R in the device is given with the use of the Dyson equations by

$$G^< = G^R(\Sigma^{<B} + \Sigma^<)G^{R\dagger}, \tag{11}$$

$$G^R = (E_z - H_0^D - \Sigma^{RB} - \Sigma^R)^{-1}, \tag{12}$$

where $G^<$ *etc.* are matrices comprised of the matrix elements defined in Eq.(10), $\Sigma^{<B}$ and Σ^{RB} are boundary self-energies, $\Sigma^<$ and Σ^R are self-energies for scattering. The boundary self-energies are related to material parameters and boundary conditions in the reservoirs, where the existence of the evanescent modes can be duly taken into account using the solution of Eq.(3)[5, 8]. We confine ourselves to polar longitudinal optical phonon (POP) and interface-roughness (IR) scatterings. Then the matrix element of the POP scattering self-energy is given by the following equation extending the expression[9, 10] into the FB space,

$$\Sigma^<_{\alpha,L;\alpha',L'} = \frac{1}{V}\sum_{\boldsymbol{q}} |U_{\boldsymbol{k}-\boldsymbol{q}}|^2 e^{iq_z\Delta(L-L'+v_{\alpha,\alpha'})} \times \left[n_{\boldsymbol{q}} G^<_{\alpha,L,\alpha',L'}(\boldsymbol{q}_\parallel; E_z - \hbar\omega) + (n_{\boldsymbol{q}}+1) G^<_{\alpha,L,\alpha',L'}(\boldsymbol{q}_\parallel; E_z + \hbar\omega)\right], \tag{13}$$

where $\boldsymbol{q}$, ω, $n_{\boldsymbol{q}}$, and $U_{\boldsymbol{k}-\boldsymbol{q}}$ denote the POP wave number, frequency, occupation number, and the electron-phonon coupling coefficient, respectively, $v_{\alpha,\alpha'}$ takes either -1/2, 1/2, or 0 for $(\alpha = c, \alpha' = a)$, $(\alpha = a, \alpha' = c)$, or otherwise, respectively. IR scattering is estimated by assuming an exponential correlation function:$\langle \Delta\boldsymbol{r}\Delta\boldsymbol{r}'\rangle = \exp(-|\boldsymbol{r}-\boldsymbol{r}'|/\Lambda)$, where Λ is assumed to be 10 nm.

By solving the equation of motion (Eq.(11)) with respect to $G^<(\boldsymbol{k}_\parallel, E_z)$, we can calculate both the electron concentration and the current density at layer L as follows,

$$n_L = -\frac{2i}{A\Delta}\sum_{\boldsymbol{k}_\parallel}\int\frac{dE_z}{2\pi}\mathbf{Tr}\left[G^<_{L,L}(\boldsymbol{k}_\parallel, E_z)\right], \tag{14}$$

$$J_L = \frac{2e}{\hbar A}\sum_{\boldsymbol{k}_\parallel}\int\frac{dE}{2\pi}2\mathbf{Re}\left\{\mathbf{Tr}\left[-t_{L,L+1}G^<_{L+1,L}(\boldsymbol{k}_\parallel, E_z)\right]\right\}$$

where A is the cross sectional area, e the electronic charge, **Tr** denotes trace of the matrix, and **Re** is real part of the physical quantity. Poisson's equation is simultaneously solved to include the space charge effect for selfconsistent calculation.

3. Results and Discussion

Figure 1 shows a comparison of the complex band structure of the AlAs barrier calculated by the conventional single band (SB) model and the FB model. Imaginary wave vectors are plotted on the left, which correspond to decay constants, whereas real wave vectors are plotted on the right. The complex modes (evanescent modes) as well as the real bands should be considered at an interface to match electron waves existing in the GaAs/AlAs heterostructure, since a disruption of translational symmetry occurs at the interface.

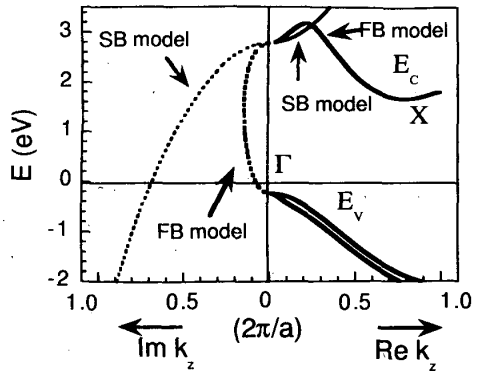

Fig. 1 Complex band structures of AlAs barrier. Those calculated by the SB model is shown for comparison.

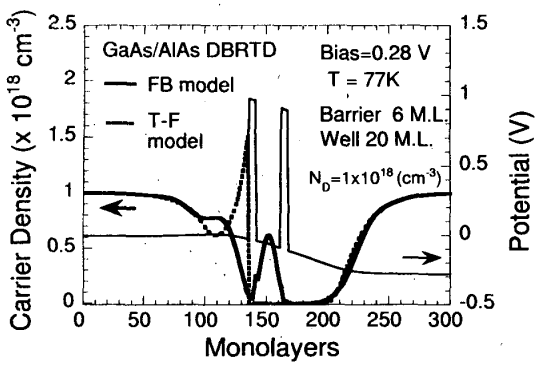

Fig. 2 Calculated band structure and carrier concentration of a GaAs/AlAs DBRTD at first resonance based on the self-consistent FB model compared with the Thomas-Fermi (T-F) model.

We focus on electron transport in a GaAs/AlAs DBRTD fabricated on (001) GaAs as schematically illustrated in Fig. 2. Barrier, well, and non-doped spacer width are 6, 20, and 35 mono-layers, respectively. Donor concentration is assumed to be 1×10^{18} cm^{-3}. Figure 2 also shows comparison of the carrier concentration profiles calculated self-consistently by the FB model and the Thomas-Fermi (T-F) model under a resonant condition ($V_B = 0.28V$). Because the T-F model [11, 12] assumes three dimensional density of states throughout the devices, there are little electrons in the well and much accumulation of electrons at the left electrode-barrier interface. However, due to the quantization in these regions, energies close to the local conduction band edge are not allowed, that is, we can no longer use three dimensional density of states in these regions. On the other hand, the present Green's function method can treat the quantum size effect naturally at any bias condition. The results indicate that the conventional T-F assumption is no longer valid and the space charge effect may significantly change the results of tunneling characteristics.

The FB model includes the transport via Γ-X (or reverse) channel. Figure 3 shows a comparison of the transmission coefficient for electrons with $E = 0.1 \cdot E_F$ between the FB model and the SB model. The SB model shows only one resonant peak due to the Γ-Γ tunneling at a voltage around 0.32 V. On the other hand the FB model shows two peaks, the latter of which is due to the Γ-X resonance, in addition, two anti-resonance dips.

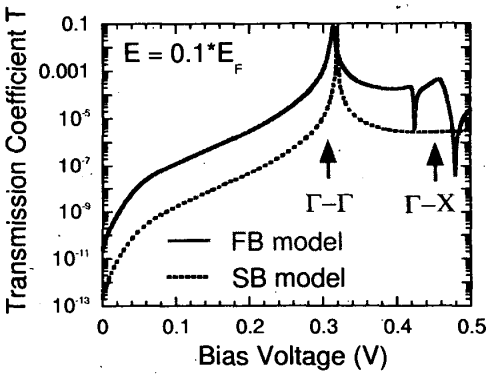

Fig. 3 Transmission coefficient as a function of the bias voltage. The incident electron energy is assumed 10% of the Fermi energy (E_F)in the left reservoir. Solid line is calculated by the FB model and dashed line SB model. The first arrow indicates the Γ-Γ resonance while the second the Γ-X resonance.

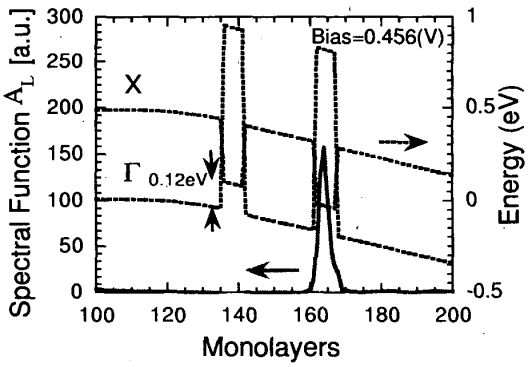

Fig. 4 Spectral function for electrons with $E = 0.1 \cdot E_F$, Γ, and X potential profile at the Γ-X resonance.

To understand the physical mechanisms at these resonant peaks, the spectral function, which has similar physical meaning of the density of states, at the second peak is drawn in Fig. 4. The first peak in Fig. 3 is due to the tunneling via Γ-level in the well,

whereas the second peak is found to be due to the resonant tunneling via X-valley resonant level in the right barrier.

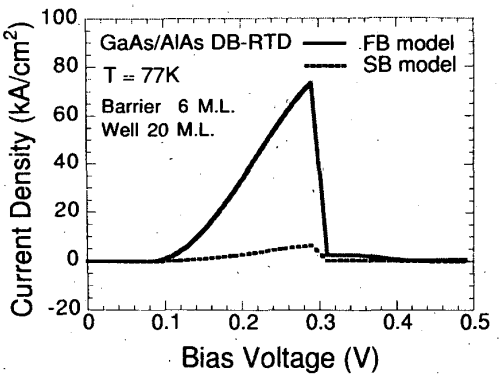

Fig. 5 I-V characteristics of the DBRTD calculated by the self-consistent tight binding full-band (FB) model (solid line) and the SB model (dashed line).

Figure 5 shows I-V characteristics of the DBRTD calculated by the FB model and the SB model, both without any scattering effects. The current densities in the FB model is larger than the SB model. The reason is that the SB model overestimates the decay constant in the barriers (see Fig.1), because it assumes a constant effective mass. On the other hand, the FB model can reflect the realistic band structures both in the real and the imaginary bands, and has a smaller decay constant, which results in the larger current densities. The FB model can include the transport via a Γ-X channel, however, such channel does not play a crucial role to increase the current density drastically in the present structure, since we have assumed thin AlAs barriers (6 MLs) in our model.

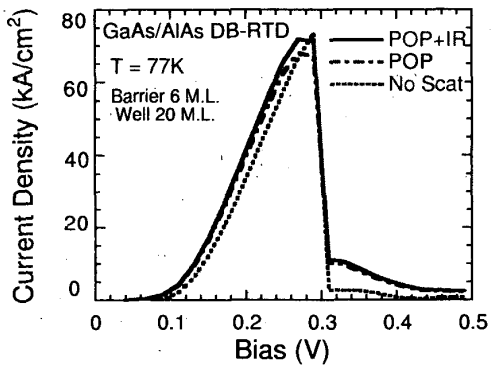

Fig. 6 Comparison of I-V characteristics including scattering mechanisms.

Figure 6 shows comparison of the I-V characteristics with POP and IR scattering taken into account in our FB model and without POP scattering. We note that the peak current is slightly increased by the POP scattering and a pronounced phonon peak is clearly observed in the valley current, which is qualitatively consistent with the experimental results[13]. Although we have to include other scattering mechanisms such as the ionized impurity scattering, acoustic phonon scattering *etc.* for quantitative comparison, the POP scattering may be the crucial scattering effect which degrades the peak-to-valley current ratio of GaAs/AlAs based DBRTDs.

4. Conclusion

We have formulated quantum transport based on the non-equilibrium Green's functions where full-band nature of realistic band structures, space charge effect, and the scattering effects are taken into account. As a result, conventional single band model is found to be inaccurate due to overestimate of decay constant in the barriers. The Thomas-Fermi assumption is found to be invalid. Although the phonon scattering effect slightly increases the peak current, it significantly increases valley current, which may be responsible for degradation of the peak to valley current ratio in most DBRTs.

References

[1] L.L. Chang, L. Esaki, and R. Tsu, Appl. Phys. Lett. **24**, (1974) 593.

[2] E.E. Mendez, E. Calleja, C.E.T Goncalves da Silv, L.L. Chang, and W.I. Wang, Phys. Rev. B**33** (1986) 7368.

[3] D. Landheer, C.H. Liu, M. Buchanan, and R. Stoner, Appl. Phys. Lett. **54** (1989) 1784.

[4] V. Heine, Proc. Phys. Soc. **81** (1963) 300.

[5] M. Ogawa, T. Sugano, and T. Miyoshi, Solid-St. Electron. **42** (1998) 1527.

[6] C. Caroli, R. Combescot, P. Nozieres, and D. Saint-James, J. Phys. C **4** (1971) 916.

[7] R. Lake, G. Klimeck, R.C. Bowen, and D. Jovanovic J. Appl. Phys. **81** (1997) 7845.

[8] M. Ogawa, T. Sugano, and T. Miyoshi, *Compound Semiconductors 1998*, ed. H. Sakaki, *Inst. Phys. Conf. Ser.* **162** (1999) 319.

[9] G.D. Mahan, Phys. Rep. **145** (1987) 251.

[10] H. Haug and S.W. Koch, *Quantum Theory of the Optical and Electronic Properties of Semiconductors*(2nd ed.), Chap. 21, World Scientific, Singapore (1993).

[11] H. Ohnishi, T. Inata, S. Muto, N. Yokoyama, and A. Shibatomi, Appl. Phys. Lett. **49** (1986) 1248.

[12] T.B. Boykin and J.S. Harris, J. Appl. Phys. **72**, (1992) 988.

[13] R. Lake, G. Klimeck, R.C. Bowen, C. Fernando, M. Leng, T.S. Moise, and Y-C. Kao, Superlatt. Microstruct. **20** (1996) 279.